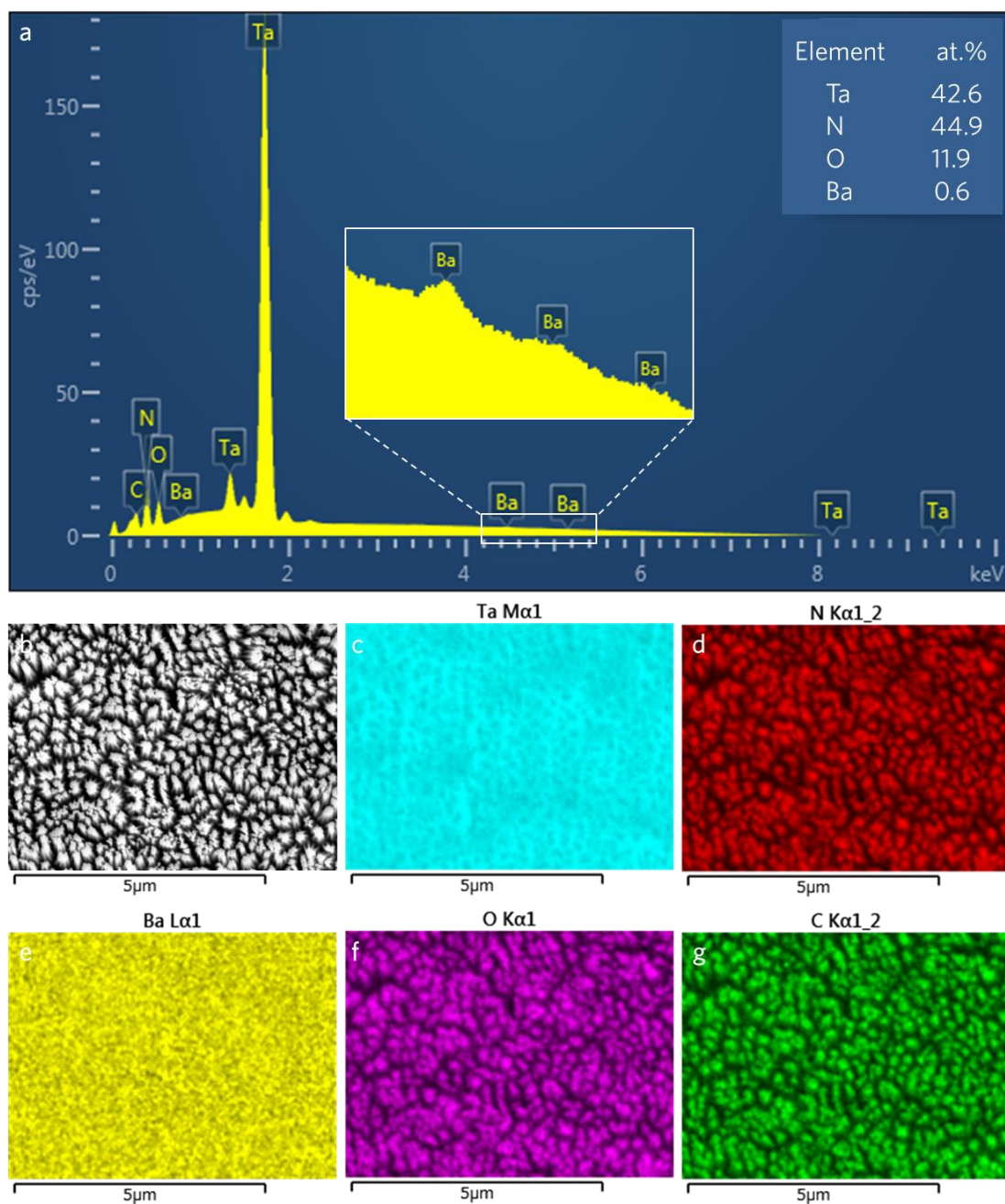
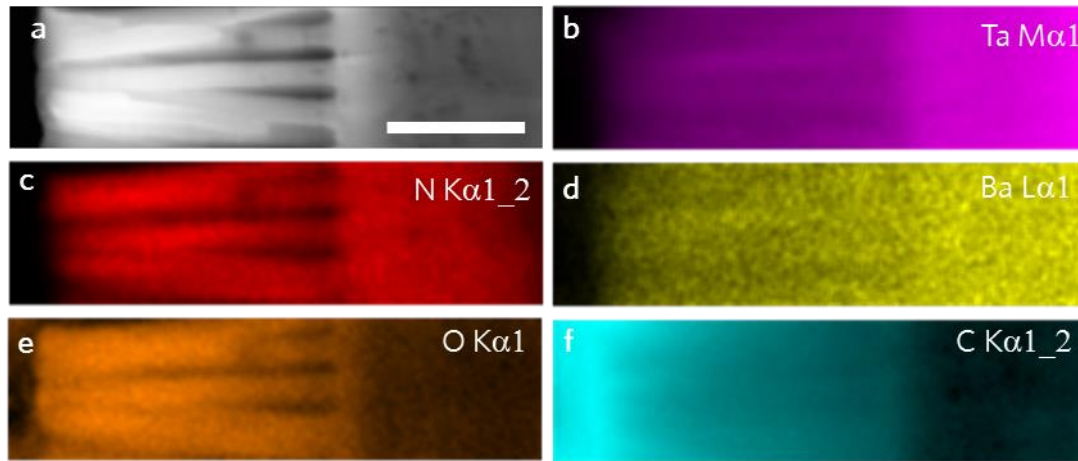


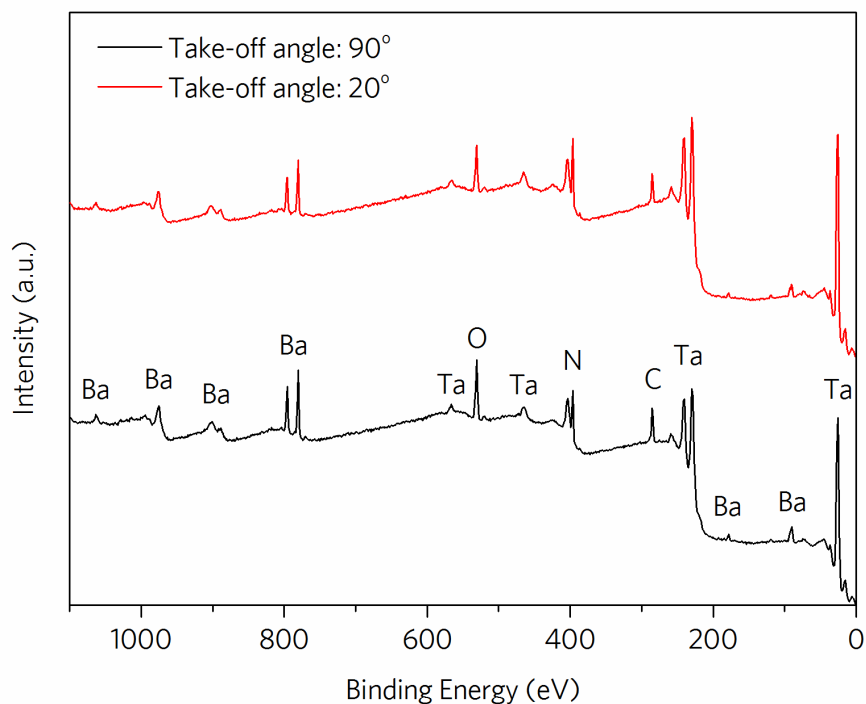
Supplementary Figure S1 | Structural properties of Ta₃N₅ and Ba-Ta₃N₅ nanorods. SEM images of a, Ta₃N₅ nanorods, and b, Ba-Ta₃N₅ nanorods. STEM images of c, d, Ta₃N₅ nanorods, and e, f, Ba-Ta₃N₅ nanorods. No obvious change in the morphology of the nanorods was found after Ba doping. Similar porous morphology was found for both Ta₃N₅ and Ba-Ta₃N₅ nanorods. The pores in the nanorods were formed likely due to the decrease of volume when Ta₂O₅ was transformed into Ta₃N₅. The scale bars: a and b, 200 nm, c, 50 nm, d, 10 nm, e, 50 nm, f, 20 nm.



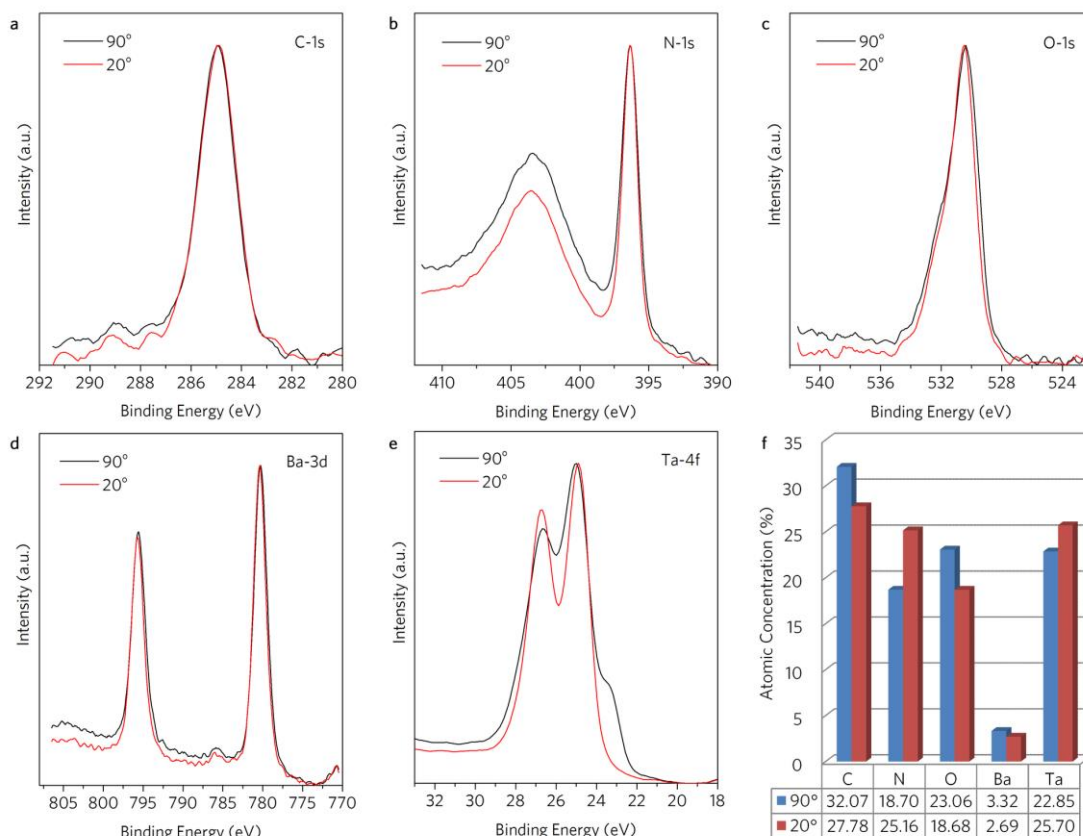
Supplementary Figure S2 | EDS analyses of Ba-Ta₃N₅ nanorods. **a**, EDS spectrum of the area shown in **b**. The magnified view of the spectrum shown in the inset clearly revealed the Ba signals. The atomic concentrations of the elements revealed by EDS analysis were given in the top-right corner. **b**, SEM image of the Ba-Ta₃N₅ nanorods used for EDS analyses. **c-g**, Elemental mapping of the area in **b** for Ta, N, Ba, O, and C, respectively. The elemental mapping revealed uniform distribution of Ba on the surface of the sample.



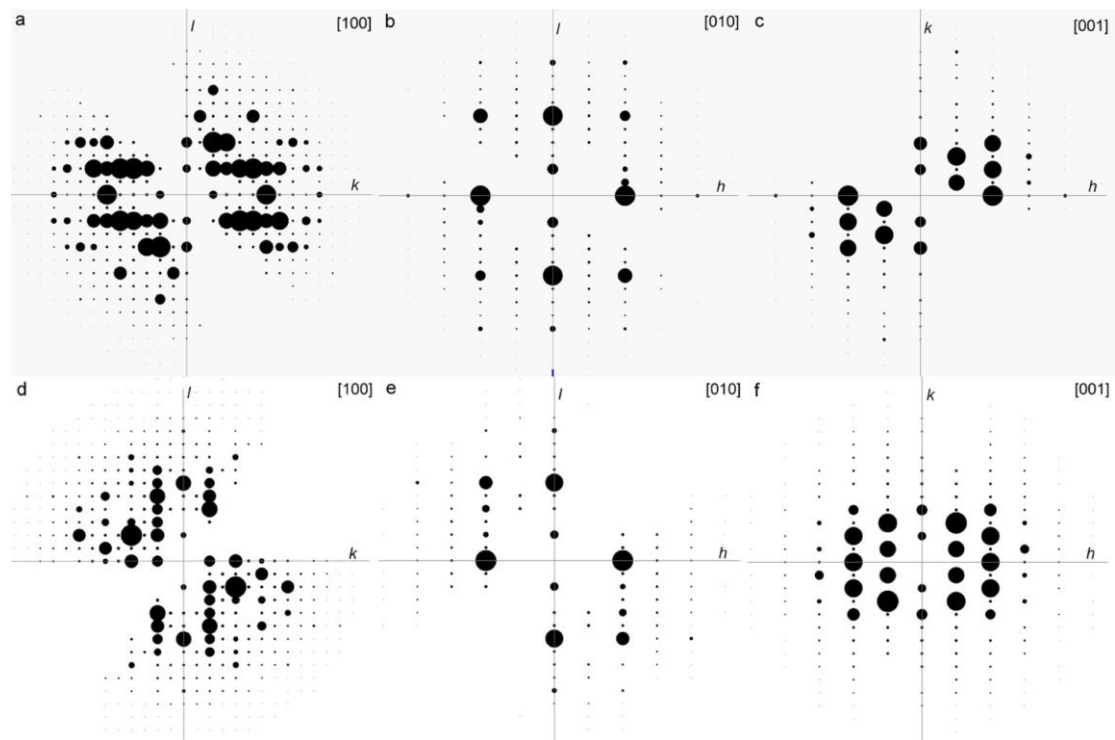
Supplementary Figure S3 | EDS mapping of cross section of the Ba-Ta₃N₅ sample. **a**, SEM image of the mapped area. The scale bar is 300 nm. **b-f**, Elemental mapping of the area in **b** for Ta, N, Ba, O, and C, respectively. The elemental mapping of the cross section of the sample revealed that Ba not only located on the surface of sample, but also entered the sample.



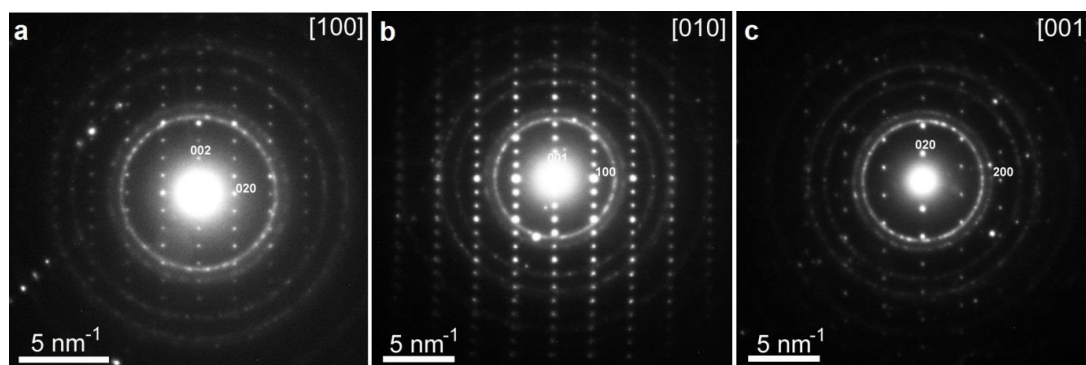
Supplementary Figure S4 | Wide-scan XPS survey spectra in the Ba-Ta₃N₅ sample. The black curve was measured at a take-off angle of 90°. To reduce the influence of the substrate on the XPS signal, the XPS spectrum was also measured at a take-off angle of 20° (red curve). Charging shift compensation was made for both curves using C-1s at 285 eV as the reference. Both curves clearly revealed peaks from Ba, in addition to those from Ta, N, O, and C.



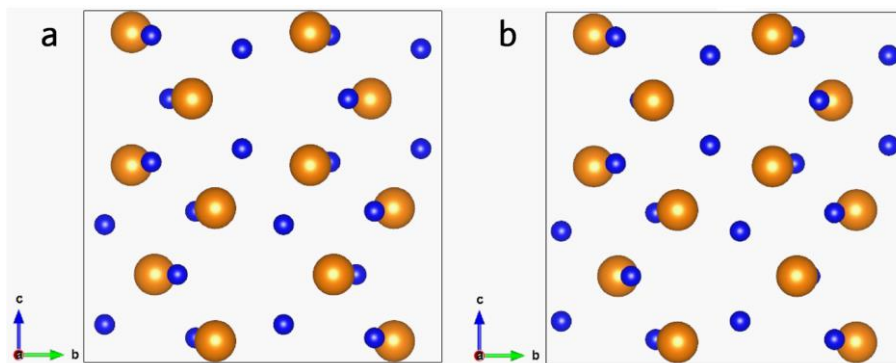
Supplementary Figure S5 | Narrow-scan XPS spectra of all elements in the Ba-Ta₃N₅ sample and quantitative analysis. a-e, Narrow-scan XPS spectra of C, N, O, Ba, and Ta measured at take-off angles of 90° (black curves) and 20° (red curves). Charging shift compensation was made for all curves using C-1s at 285 eV as the reference. The intensity of the peaks measured at different take-off angles were normalized for comparison. f, Atomic concentrations of C, N, O, Ba, and Ta estimated from quantitative XPS analysis for take-off angles of 90° (blue bars) and 20° (red bars). The atomic concentrations estimated from the spectra taken at a small take-off angle of 20° were likely closer to the actual atomic concentrations on the surface of the nanorods since they were less affected by the substrate.



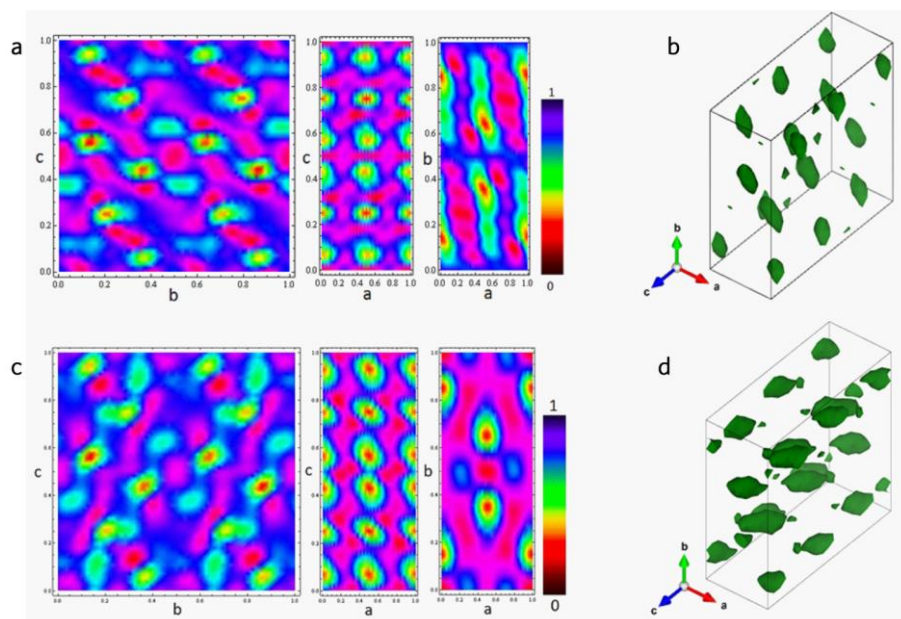
Supplementary Figure S6 | 3D-EDT for the Ta_3N_5 and $\text{Ba-Ta}_3\text{N}_5$ nanorods. Slices of 3D reciprocal lattices for **a-c**, Ta_3N_5 and **d-e**, $\text{Ba-Ta}_3\text{N}_5$ nanorods along [100], [010] and [001] zone axes, respectively. Note, information from some reciprocal space is missing because of missing cone in data collection through 3D-EDT. The two reconstructed reciprocal lattices present same Laue class of mmm and C -center Bravais lattice type. From these patterns, reflection condition rules can be summarized as $\{hkl: h+k=2n; Okl: k=2n; hOl: h,l=2n\}$, which certify the space group of $Cmcm$. Accurate unit cell parameters were calculated to be $a=3.62 \text{ \AA}$, $b=10.04 \text{ \AA}$, and $c=9.86 \text{ \AA}$ by internal standard method with the help of gold nanoparticles coating.



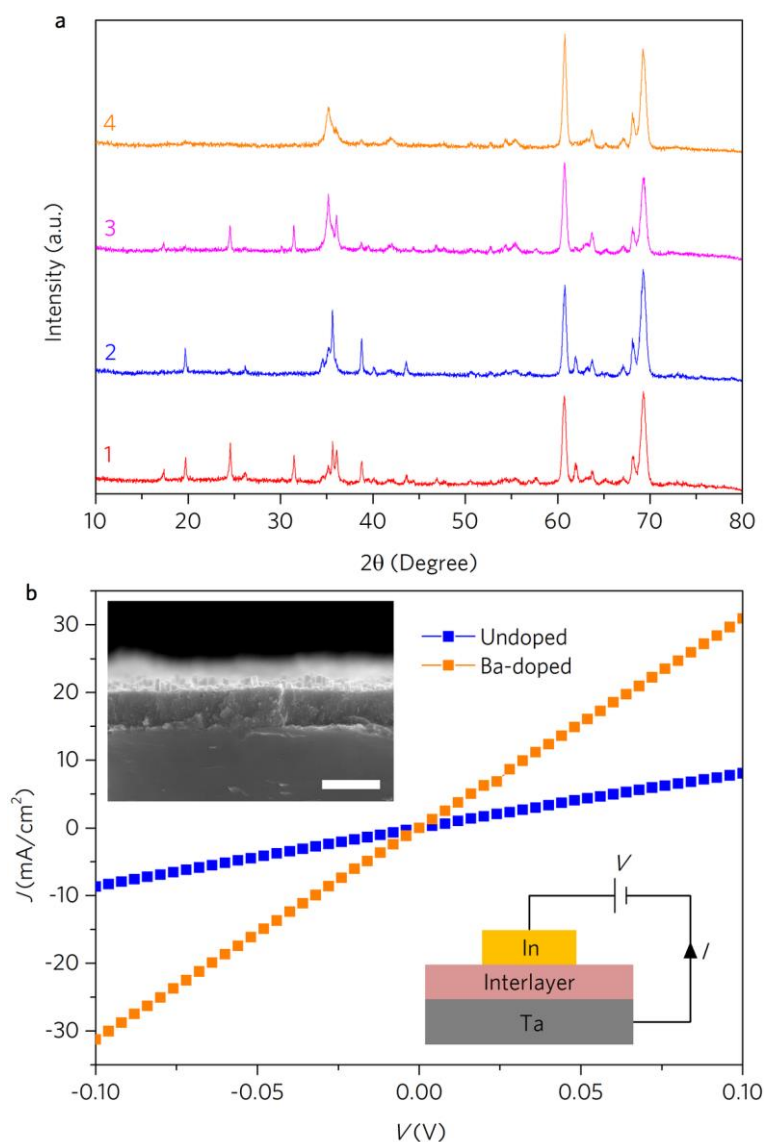
Supplementary Figure S7 | Selected area electron diffraction (SAED) patterns of Ba-Ta₃N₅ nanorods along [100], [010] and [001]. Accurate unit cell parameters were determined as $a=3.62$ Å, $b=10.04$ Å and $c=9.86$ Å by internal calibration method with the help of sputtered gold nanoparticles on the nanorods. The four Debye rings corresponding to 111, 200, 220 and 311 reflections were observed from Au nanoparticles.



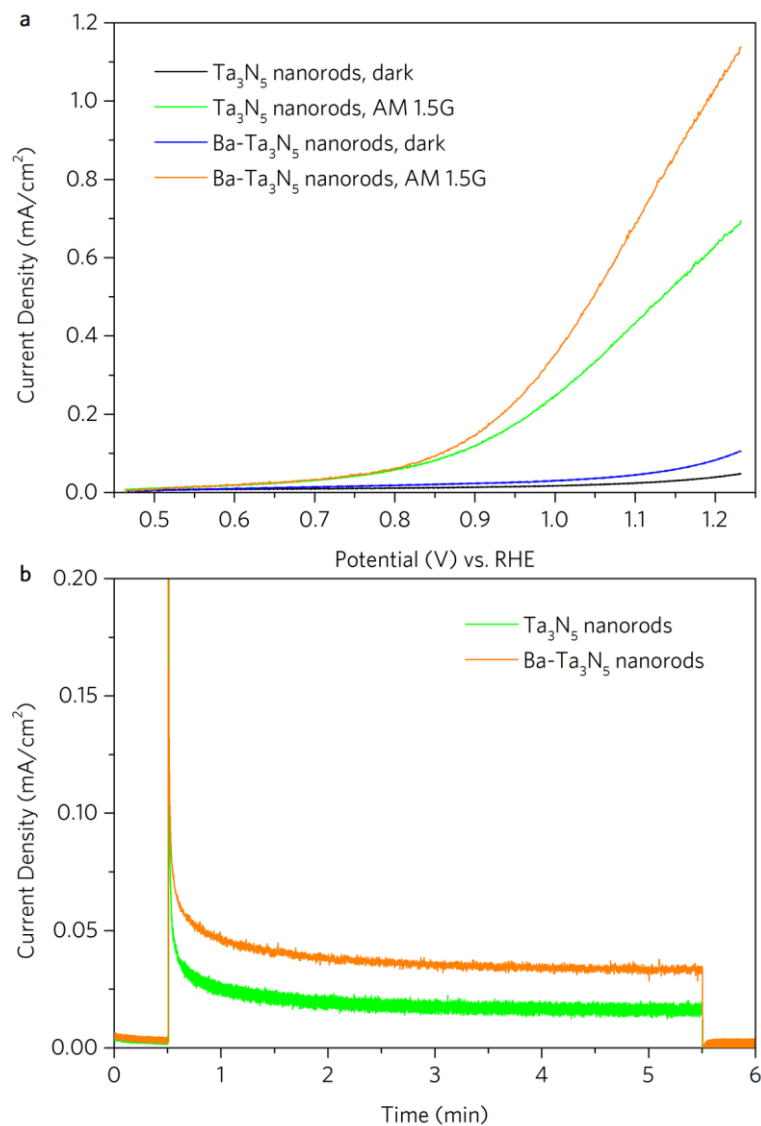
Supplementary Figure S8 | Projection of structural model for a, Ta_3N_5 and b, $\text{Ba-Ta}_3\text{N}_5$ along [100]. Ta: orange sphere; N: blue sphere. The ab initio structure solutions of crystals were solved using direct method in *Sir2011*, which reveals very similar atomic arrangements between the two samples.



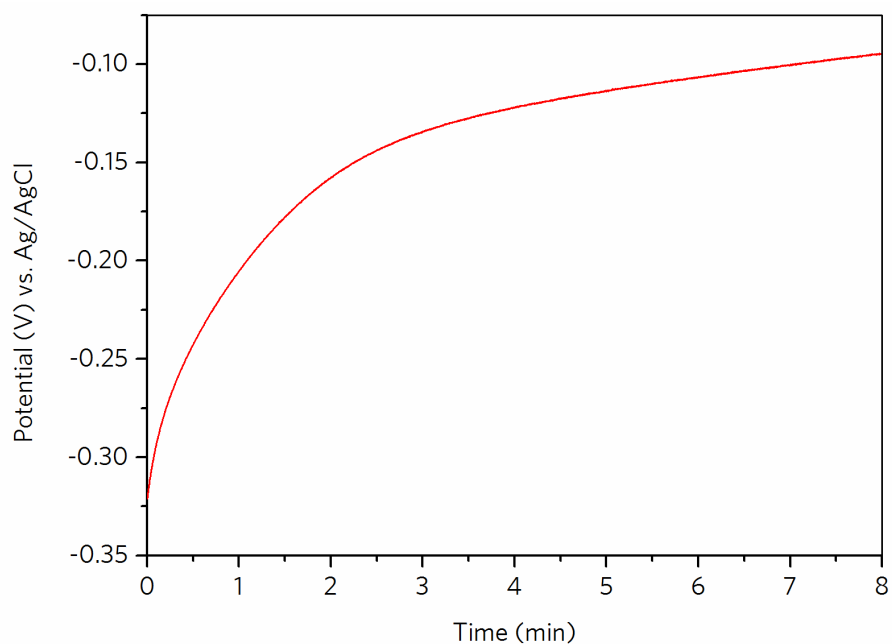
Supplementary Figure S9 | Electrostatic potential map (EPM) reconstructed by Fourier synthesis of crystal structure factors obtained for electrons. a and c, 2D electrostatic potential projection along [100], [010] and [001] zone axes for Ta_3N_5 and Ba- Ta_3N_5 ; b and d, 3D electrostatic potential map with threshold value of 0.63 for Ta_3N_5 and Ba- Ta_3N_5 . The 3D EPM and 2D projections present similar features except for the orientation of electrostatic distributions. Plots of EPM show little differences between these two structures. All the Ta and N atoms can be located properly on basis of their EPM distribution. Moreover, slightly higher distribution at some N atom locations in Ba- Ta_3N_5 structure might reveal mixed existence of O atoms with larger atomic number, which could be certified in electron energy loss spectroscopy (EELS) and energy-dispersive X-ray spectroscopy (EDS) analyses. However, it is difficult to distinguish mixture of O and N at the same position by 3D EDT data due to its higher dynamic effects and experimental errors compared with single X-ray. Mixture of occupancy for N/O atoms does not improve refinement of the structures (R factors are 26.5% for Ta_3N_5 and 26.7% for Ba- Ta_3N_5).



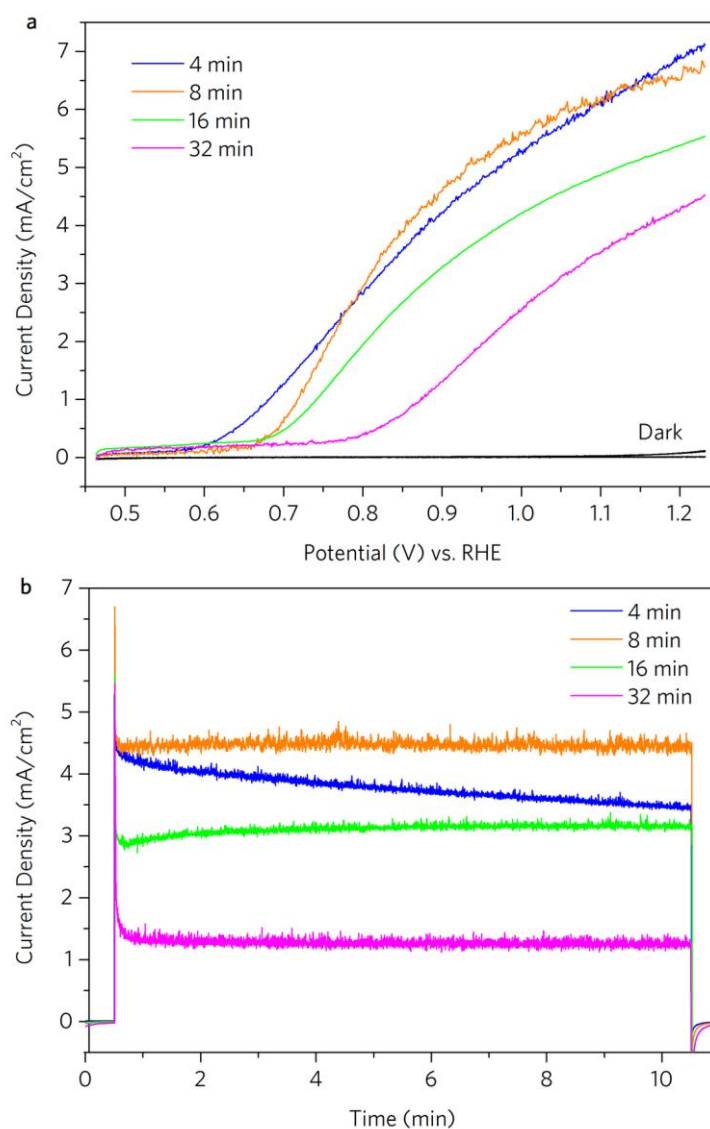
Supplementary Figure S10 | Structural and electrical properties of the interlayers of the undoped and Ba-doped samples. The nanorods were removed from the substrates by extensive sonication in water. **a**, XRD patterns of the undoped (curves 1 & 2) and Ba-doped (curves 3 & 4) samples before (curves 1 & 3) and after (curves 2 & 4) removing the nanorods, which revealed that the Ta_5N_6 phase existed in the interlayer of the undoped sample and was suppressed by Ba doping. **b**, I - V curves of the interlayers of the undoped and Ba-doped samples. Top-left inset shows the SEM image of sample after removing the nanorods. The scale bar is 500 nm. Bottom-right inset shows the schematic drawing of the structure for I - V measurement. Indium thin film with a thickness of ~ 500 nm was evaporated on the surface through a shadow mask as top electrode. Both samples showed linear I - V curves. However, the conductivity of the Ba-doped sample was approximately 3 times higher than the undoped sample.



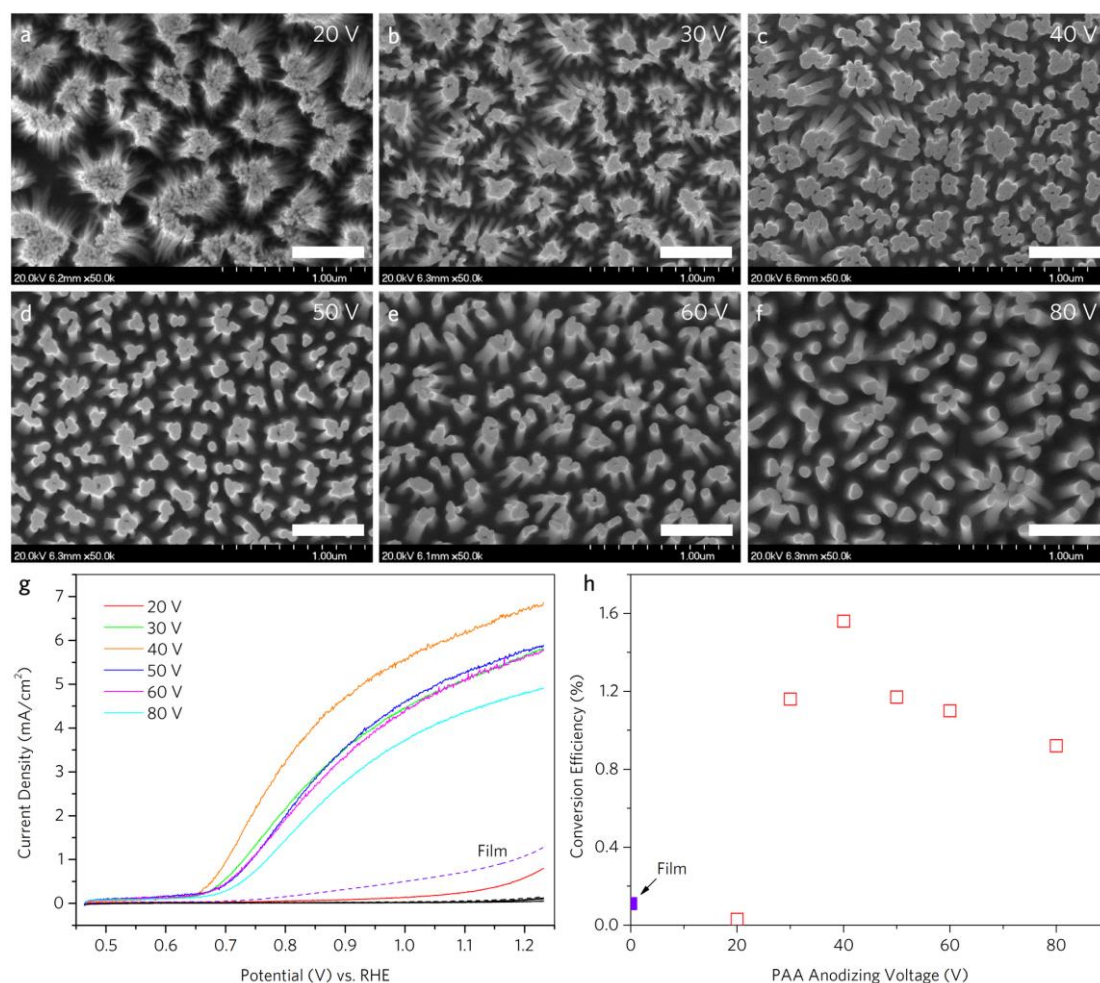
Supplementary Figure S11 | PEC water splitting properties of bare Ta₃N₅ and Ba-Ta₃N₅ nanorods. **a**, Current-potential curves of Ta₃N₅ and Ba-Ta₃N₅ nanorods without modifying Co-Pi co-catalyst. **b**, Stability of the photocurrent of the bare Ta₃N₅ and Ba-Ta₃N₅ nanorod photoanodes held at 0.9 V vs. RHE under AM 1.5G. The electrolyte was 0.5 M K₂HPO₄ at pH 13. Without modifying Co-Pi co-catalyst, the photocurrent densities were much lower than the Co-Pi modified samples and the photocurrent decayed rapidly upon illumination for both undoped and Ba-doped samples.



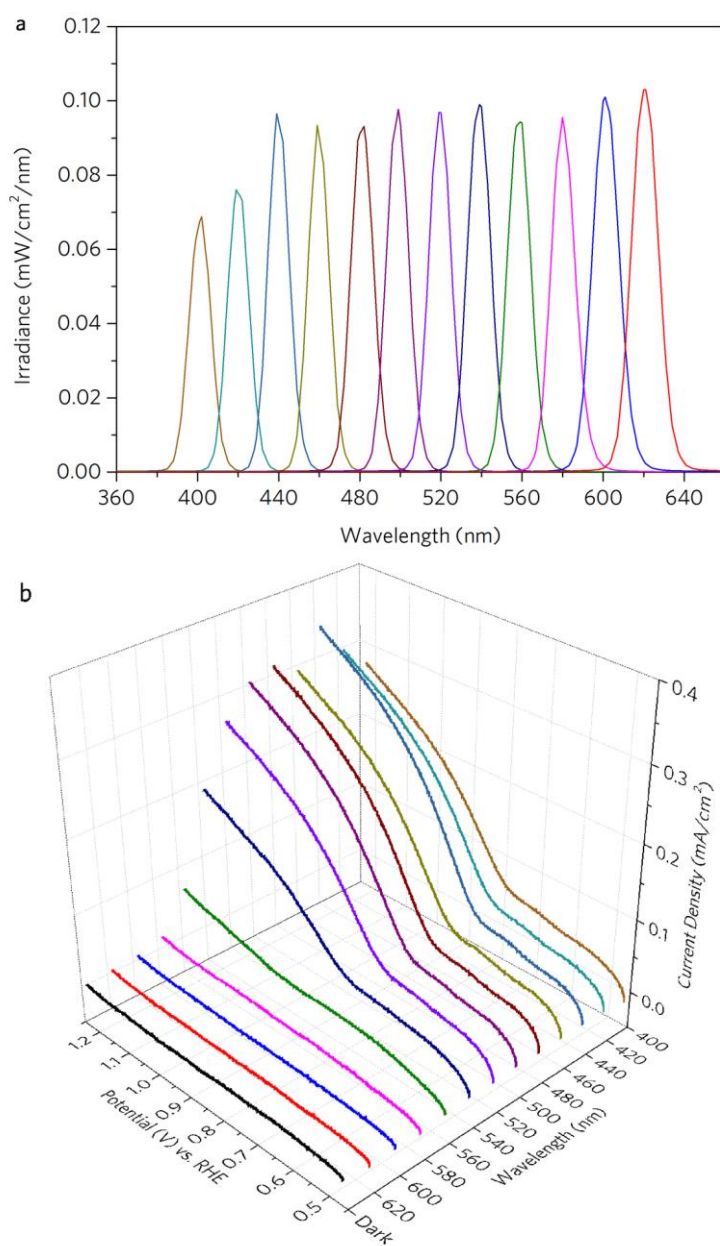
Supplementary Figure S12 | Voltage profile of the Ba-Ta₃N₅ nanorod electrode for photo-assisted electrodeposition of Co-Pi at a constant current density of 10 $\mu\text{A}/\text{cm}^2$. The electrodeposition was carried out in 0.5 mM Co(NO₃)₂ in a 0.1 M potassium phosphate buffer at pH = 7 under stirring and AM 1.5G irradiation. Deposition at a constant and low current density allowed the Co-Pi to be deposited uniformly on the nanorod surface.



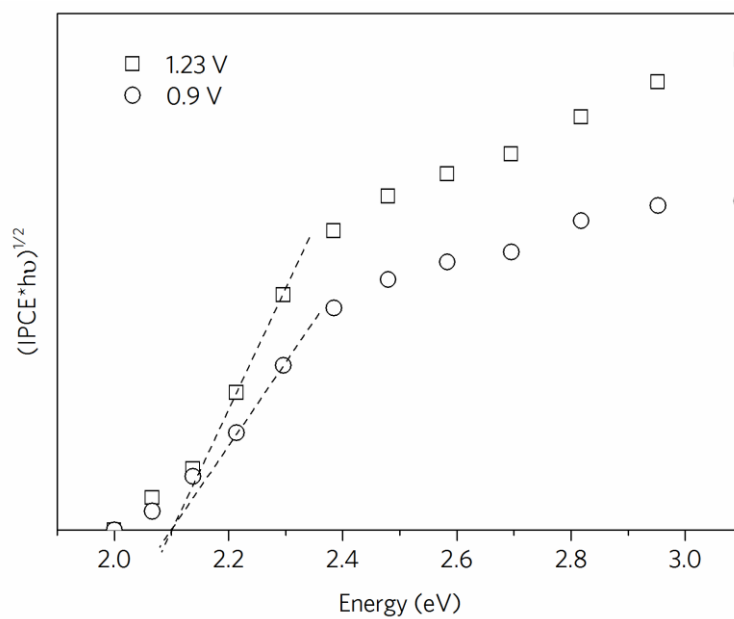
Supplementary Figure S13 | PEC water splitting properties of Ba-Ta₃N₅ nanorods modified with different amount of Co-Pi co-catalysts. The amount of Co-Pi co-catalysts modified on the samples were varied by controlling the time (4-32 min) for the photo-assisted electrodeposition at a constant current density (10 $\mu\text{A cm}^{-2}$). **a**, Current-potential curves of Ba-Ta₃N₅ nanorods modified with different amount of Co-Pi co-catalysts in the dark (black curves) and under AM 1.5G (colored curves) in 0.5 M K₂HPO₄ at pH 13. **b**, Stability of the photocurrent of the Ba-Ta₃N₅ nanorods modified with different amount of Co-Pi co-catalysts held at 0.9 V vs. RHE under AM 1.5G. Deposition for 8 min was found to be the best time among those we tested. Increasing the Co-Pi amount would decrease the activity, while decreasing the Co-Pi amount would decrease the stability, although the initial activity was still high.



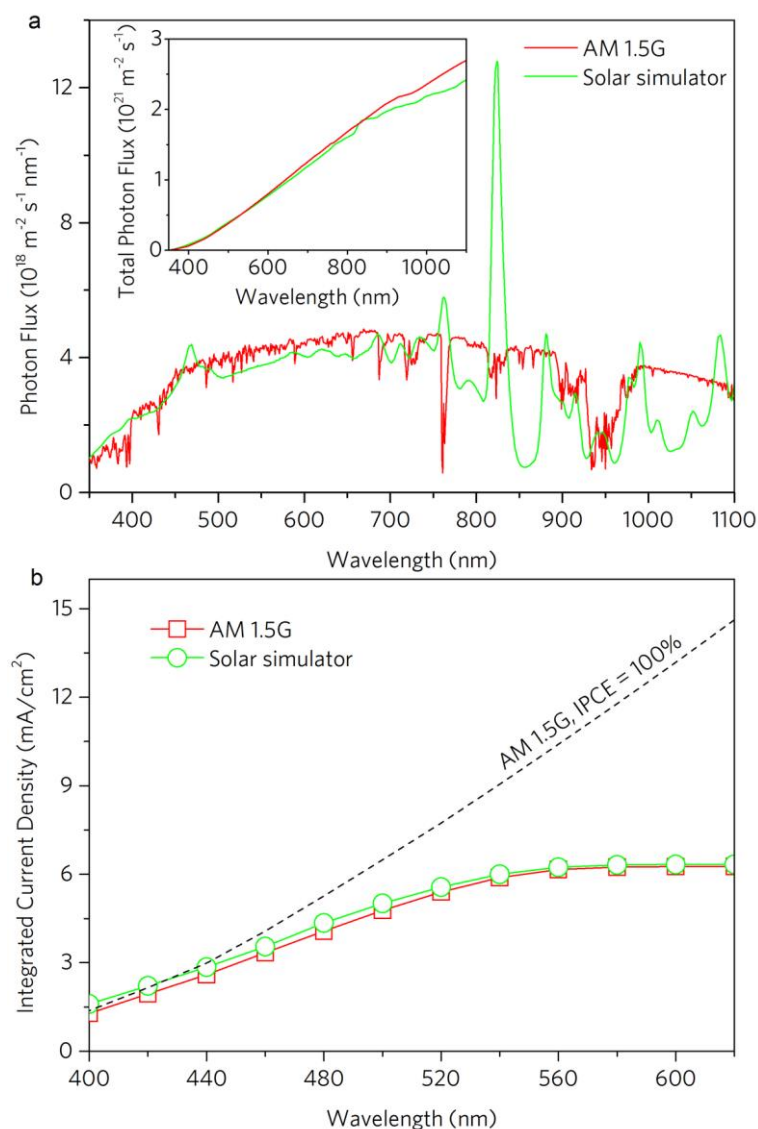
Supplementary Figure S14 | Effect of the anodizing voltage for PAA mask on the PEC water splitting properties of Co-Pi/Ba-Ta₃N₅ nanorods. By changing the anodizing conditions of the PAA masks (Table S2), the diameter and the density of the nanorods can be varied. **a-f**, SEM images of the Ba-Ta₃N₅ nanorods fabricated with different PAA anodizing voltages in the range of 20-80 V. The scale bars are 500 nm. **g**, Current-potential curves of the Ba-Ta₃N₅ nanorods fabricated with different PAA anodizing voltages in the dark (black lines) and under AM 1.5G simulated sunlight (colored lines) in 0.5 M K₂HPO₄ at pH 13. A Ba-Ta₃N₅ compact film (~800 nm in thickness) fabricated without using PAA mask was also used for comparison (dashed line). The samples were all modified with Co-Pi under the same condition. **h**, Plot of the solar energy conversion efficiencies of the Ba-Ta₃N₅ nanorod photoanodes against the PAA anodizing voltages. The closed square shows the conversion efficiency of the compact film. The activity of the sample fabricated under 20 V was even lower than that of the compact film. The exceptionally low efficiency of this sample was likely because the diameters of the nanorods were too small to sustain band bending in the nanorods.



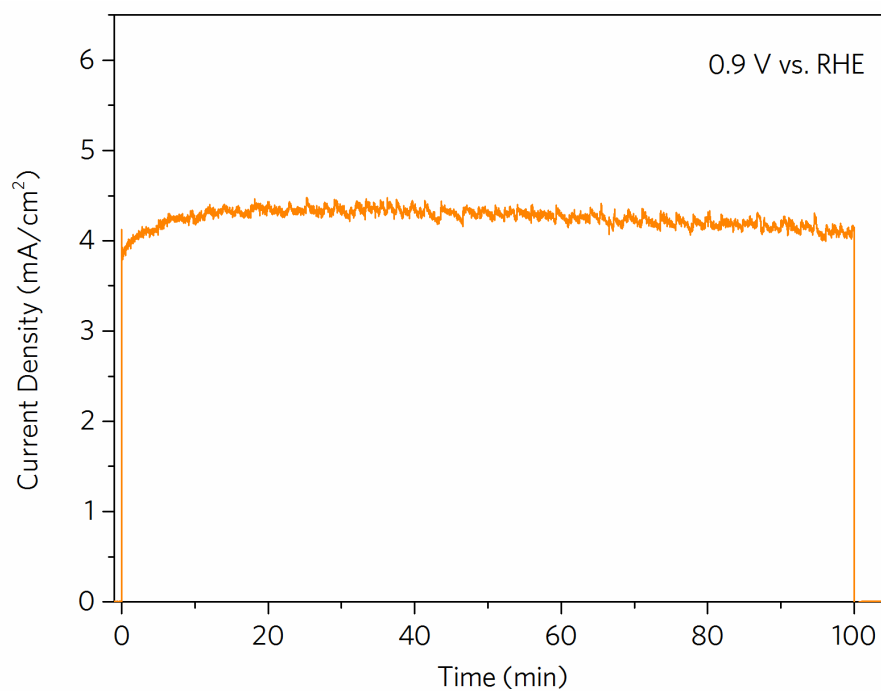
Supplementary Figure S15 | Irradiance spectra and current-potential curves measured for the calculation of IPCEs. a, Irradiance spectra of the light incident on the electrode surface. The light intensities at all wavelengths are about 1-2 mW cm⁻². **b**, Current-potential curves in the dark and under monochromatic irradiation at each wavelength. The IPCE at each wavelength (λ) was calculated via the equation $IPCE = [(1240 / \lambda) \times (J_{light} - J_{dark}) / P_{light}] \times 100\%$.



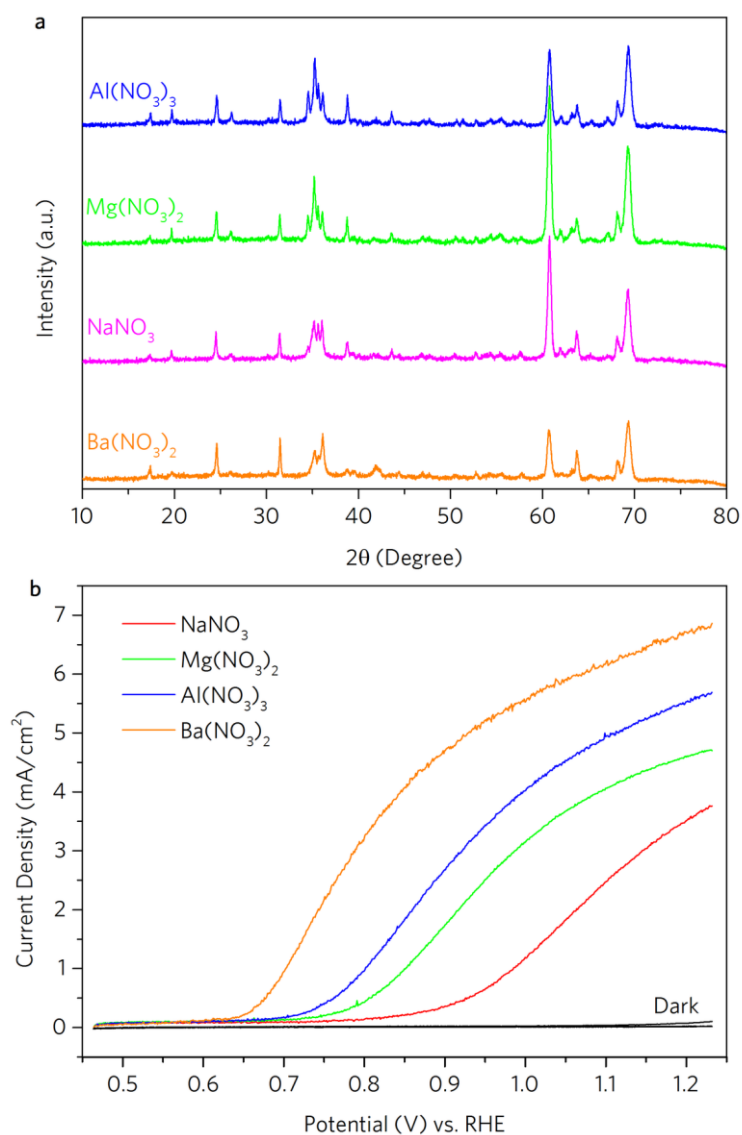
Supplementary Figure S16 | Tauc plots of the IPCE data measured at 0.9 and 1.23 V vs. RHE in Fig. 3d. The Tauc plots reveal that the band gap of the Ba-Ta₃N₅ nanorods is 2.1 eV, same as that of the undoped Ta₃N₅ reported in the literatures.



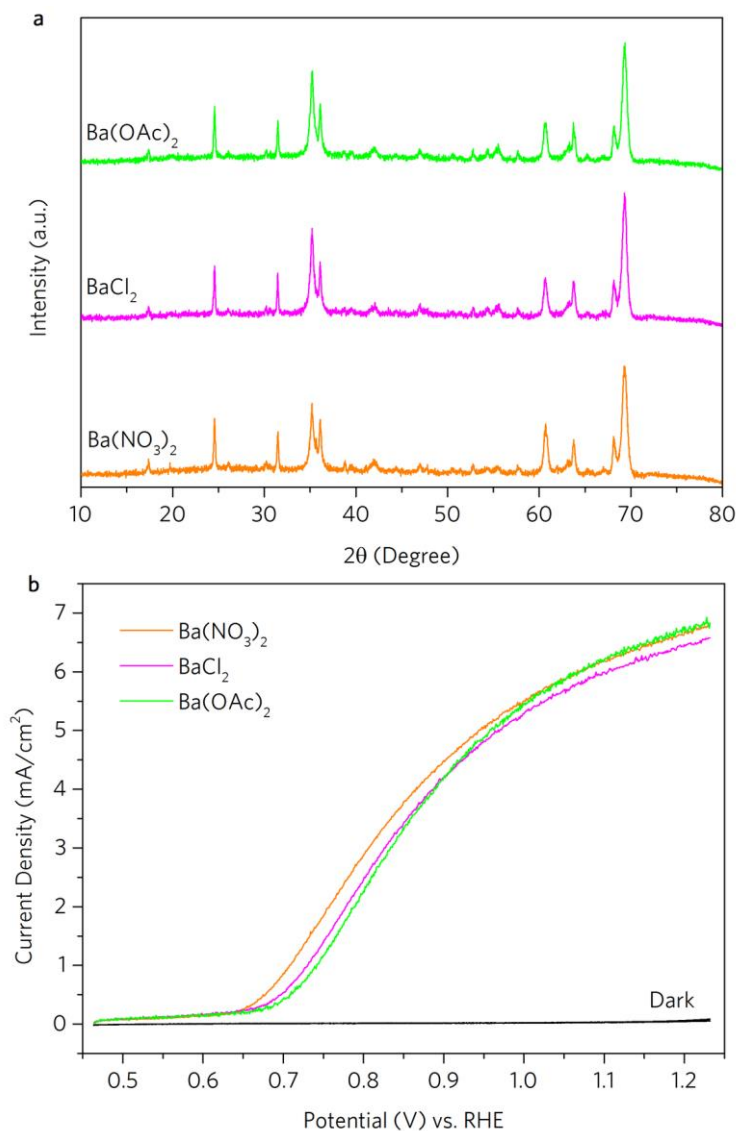
Supplementary Figure S17 | Properties of the solar simulator. a, Spectral photon flux of the AM 1.5G (ASTM G173-03) and the solar simulator. Inset shows the total photon flux in the range of 350-1100 nm for AM 1.5G and the solar simulator. The two curves match well in the spectral range below ~ 800 nm. **b**, Estimated photocurrent densities by integrating the IPCE data obtained at 1.23 V vs. RHE in Fig. 3d over the spectra of the AM 1.5G and the solar simulator. Photocurrent densities of $\sim 6.3 \text{ mA cm}^{-2}$ were estimated at 620 nm for both spectra, which were close to the value ($\sim 6.7 \text{ mA cm}^{-2}$) measured from the current-potential curve in Fig. 3a. The dashed line shows the theoretical limit of the photocurrent densities calculated by using IPCE = 100% and integrating over AM 1.5G. The difference between the solid and dashed lines indicates the potential for further improvement, especially at longer wavelengths.



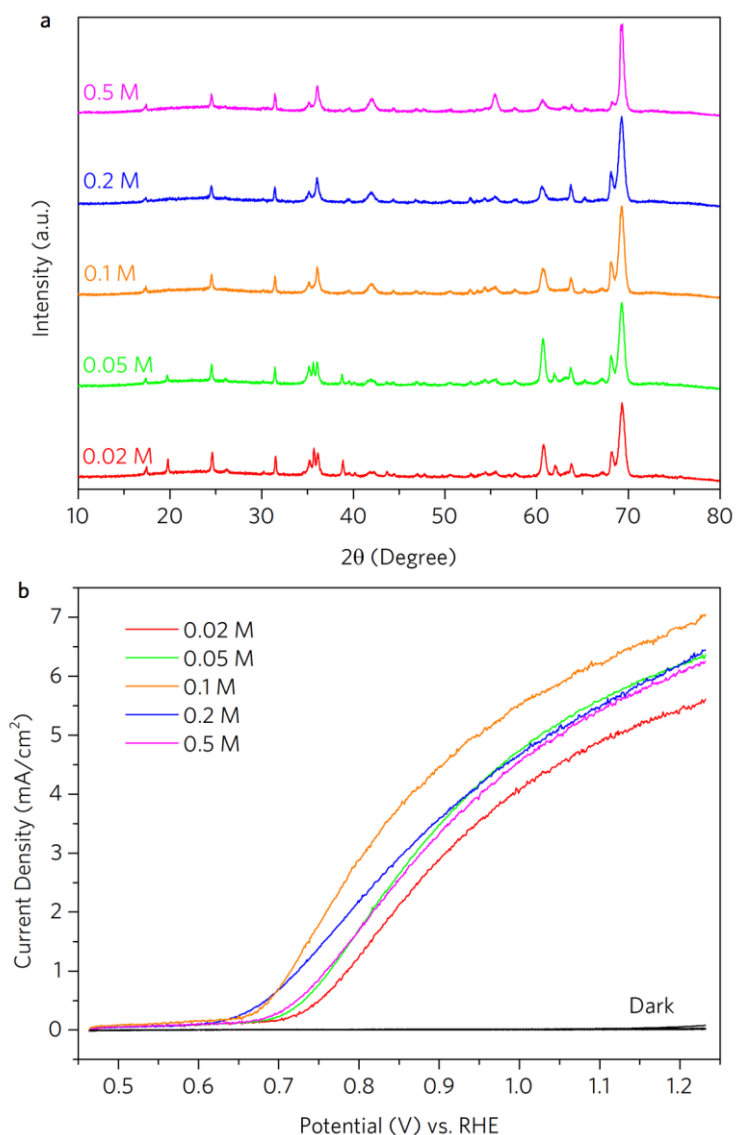
Supplementary Figure S18 | Current recorded during the gas chromatography measurement. The Co-Pi/Ba-Ta₃N₅ nanorod photoanode was held at 0.9 V vs. RHE in 0.5 M K₂HPO₄ (pH = 13) under AM 1.5G simulated sunlight for 100 min. The amount of electrons integrated from the curve during the 100 min is 265 $\mu\text{mol cm}^{-2}$. The photocurrent decays by only 5% of the maximum value after testing for 100 min.



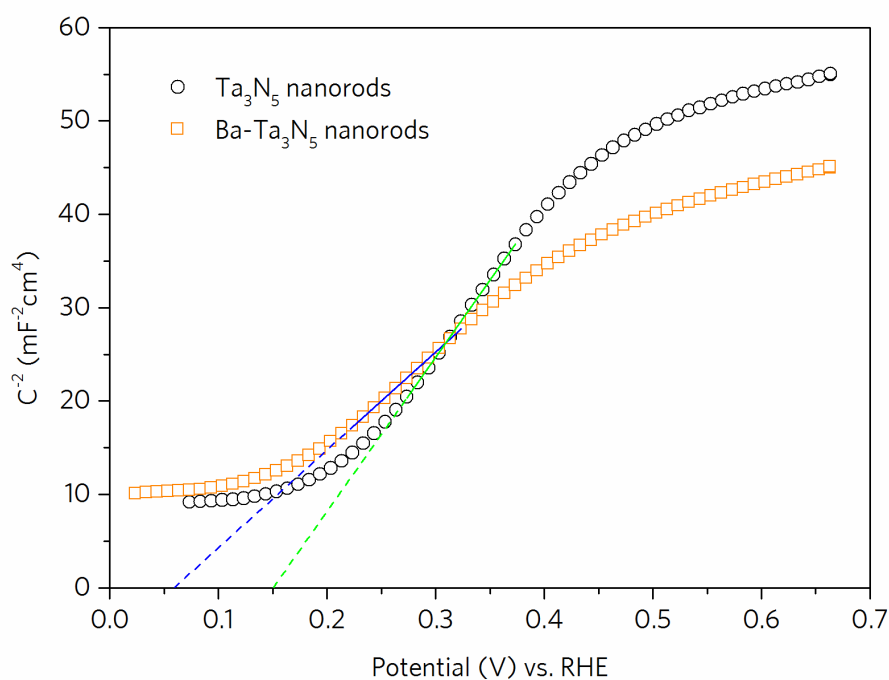
Supplementary Figure S19 | Effect of different nitrate precursors on the PEC water splitting activity of nanorod photoanodes. Aqueous solutions of the $\text{Ba}(\text{NO}_3)_2$, NaNO_3 , $\text{Mg}(\text{NO}_3)_2$, and $\text{Al}(\text{NO}_3)_3$ were used. The concentrations of the NO_3^- in these solutions were kept at 0.2 M. **a**, XRD patterns of the samples treated with different nitrate salts. The suppression of Ta_5N_6 phase was only found in the sample treated with $\text{Ba}(\text{NO}_3)_2$. **b**, Current-potential curves of samples treated with different nitrate precursors in the dark (black curves) and under AM 1.5G (colored curves) in 0.5 M K_2HPO_4 at pH 13. All the samples were modified with Co-Pi co-catalysts under the same condition. Compared with undoped sample in Fig. 3a, the NaNO_3 and $\text{Mg}(\text{NO}_3)_2$ treated samples showed even lower activity, while the $\text{Al}(\text{NO}_3)_3$ treated sample showed only slightly enhanced activity, not comparable to the $\text{Ba}(\text{NO}_3)_2$ treated sample.



Supplementary Figure S20 | Effect of different Ba precursors on the PEC water splitting activity of Co-Pi/Ba-Ta₃N₅ photoanodes. 0.1 M aqueous solutions of the Ba(NO₃)₂, BaCl₂, and barium acetate (Ba(OAc)₂) were used. **a**, XRD patterns of the samples treated with different Ba precursors. The suppression of Ta₅N₆ phase was found in all samples. **b**, Current-potential curves of samples treated with different Ba precursors in the dark (black curves) and under AM 1.5G (colored curves) in 0.5 M K₂HPO₄ at pH 13. All samples showed similar PEC activity, which were much enhanced compared with undoped sample in Fig. 3a.



Supplementary Figure S21 | Effect of concentration of Ba(NO₃)₂ precursor on the PEC water splitting activity of Co-Pi/Ba-Ta₃N₅ photoanodes. a, XRD patterns Ba-Ta₃N₅ nanorods treated with different concentrations (0.02-0.5 M) of Ba(NO₃)₂ precursor. With increasing Ba(NO₃)₂ concentration, the peaks for Ta₅N₆ decreased and finally disappeared. However, an impurity peak at ~42° also became stronger with increasing concentration. **b**, Current-potential curves of Co-Pi/Ba-Ta₃N₅ nanorods fabricated with different Ba(NO₃)₂ concentrations in the dark (black curves) and under AM 1.5G (colored curves) in 0.5 M K₂HPO₄ at pH 13. The Ba(NO₃)₂ concentration of 0.1 M was the best value among those we tested.



Supplementary Figure S22 | Mott-Schottky plots of Ta₃N₅ nanorods and Ba-Ta₃N₅ nanorods. The data was obtained by performing a potential scan in the anodic direction under a frequency of 1 kHz and an AC amplitude of 15 mV in 0.5 M K₂HPO₄ at pH = 13. Before the measurement, each sample was freshly etched with HF:HNO₃:H₂O (1:2:7 in v/v) for 10 s and rinsed with pure water. The electrolyte was stirred and purged with Ar for 20 min. Cyclic voltammetry was performed repeatedly to clean the surface of the electrode. The Mott-Schottky measurement was carried out under dark conditions. The lines show the fitting of the linear regions of the Mott-Schottky plots. From the interceptions of the lines with the x-axis, the flat-band potentials of the two samples were obtained, ~0.15 V vs. RHE for the undoped Ta₃N₅ nanorods and ~0.06 V vs. RHE for the Ba-Ta₃N₅ nanorods. The cathodic shift of the flat band potential could contribute to the improved PEC water splitting activity of the Ba-Ta₃N₅ nanorods over the Ta₃N₅ nanorods. From the slope (k_{MS}) of the lines, the carrier concentration (N_D) in the samples could be estimated from the equation $N_D = 2(\varepsilon\varepsilon_0k_{MS}f_r^2)^{-1}$, where ε is vacuum permittivity, ε_0 is the dielectric constant of Ta₃N₅ (~110), and f_r is the roughness factor of the nanorod electrode. f_r is estimated to be ~14.6 by considering nanorods with diameter of 60 nm, length of 600 nm, and areal density of $1.2 \times 10^{10} \text{ cm}^{-2}$. The carrier concentration in Ta₃N₅ nanorods and Ba-Ta₃N₅ nanorods are estimated to be $3.7 \times 10^{19} \text{ cm}^{-3}$ and $5.8 \times 10^{19} \text{ cm}^{-3}$, respectively.

Supplementary Table S1 | Atomic coordinates of Ta₃N₅ and Ba-Ta₃N₅.

	label	symbol	multiplicity	Wyckoff symbol	x	y	Z
Ta ₃ N ₅	Ta1	Ta5+	4	c	0.5	0.198	0.25
	Ta2	Ta5+	8	f	0	0.367	0.061
	N1	N3-	8	f	0.5	0.312	0.07
	N2	N3-	4	c	0	0.261	0.25
	N3	N3-	8	f	0.5	0.058	0.108
	Ba-Ta ₃ N ₅	label	symbol	multiplicity	Wyckoff symbol	x	y
Ta1		Ta5+	4	c	0.5	0.201	0.25
Ta2		Ta5+	8	f	0	0.367	0.062
N1		N3-	8	f	0.5	0.306	0.07
N2		N3-	4	c	0	0.237	0.25
N3		N3-	8	f	0.5	0.042	0.122

Space group: *Cmcm*. Unit cell parameters: $a=3.62$ Å, $b=10.04$ Å and $c=9.86$ Å.

Supplementary Table S2 | Anodization conditions and structural parameters of the PAA masks. The pores in PAA membrane have a hexagonally close-packed structure. The pore size and inter-pore distance can be adjusted by controlling the anodizing voltage and anodizing current density. Under low anodizing current density, the inter-pore distance (in nm) is approximately 2.5 times of the anodizing voltage (in V). The pore size can be further adjusted by etching in H₃PO₄ for a short time. The following conditions were used to fabricate PAA masks with different pore size and inter-pore distance. Hence, the diameter and areal density of the nanorods filling into the pores were varied by using these PAA masks.

Anodizing voltage (V)	Concentration of oxalic acid (M)	Etching time in H ₃ PO ₄ (s)	Pore size (nm)	Pore density (10 ⁹ cm ⁻²)	Pore areal fraction (%)
20	0.5	30	25	46	22
30	0.5	60	40	20	26
40	0.3	90	60	12	33
50	0.3	90	70	7.4	28
60	0.1	120	80	5.1	26
80	0.1	120	100	2.9	22